



Article

Cell-Biological Response and Sub-Toxic Inflammatory Effects of Titanium Dioxide Particles with Defined Polymorphic Phase, Size, and Shape

Marina Breisch ¹ , Mateusz Olejnik ² , Kateryna Loza ², Oleg Prymak ², Nina Rosenkranz ³, Jürgen Bünger ³ , Christina Sengstock ¹, Manfred Köller ¹ , Götz Westphal ³ and Matthias Eppler ^{2,*}

¹ BG University Hospital Bergmannsheil, Surgical Research, Ruhr University of Bochum, 44789 Bochum, Germany

² Inorganic Chemistry and Center for Nanointegration Duisburg-Essen (CENIDE), University of Duisburg-Essen, 45117 Essen, Germany

³ Institute for Prevention and Occupational Medicine of the German Social Accident Insurance (IPA), Institute of the Ruhr University of Bochum, 44789 Bochum, Germany

* Correspondence: matthias.eppler@uni-due.de

Abstract: Six types of titanium dioxide particles with defined size, shape, and crystal structure (polymorphic form) were prepared: nanorods ($70 \times 25 \text{ nm}^2$), rutile sub-microrods ($190 \times 40 \text{ nm}^2$), rutile microspheres (620 nm), anatase nanospheres (100 nm), anatase microspheres (510 nm), and amorphous titania microspheres (620 nm). All particles were characterized by scanning electron microscopy, X-ray powder diffraction, dynamic light scattering, infrared spectroscopy, and UV spectroscopy. The sub-toxic cell-biological response to these particles by NR8383 macrophages was assessed. All particle types were taken up well by the cells. The cytotoxicity and the induction of reactive oxygen species (ROS) were negligible for all particles up to a dose of $100 \mu\text{g mL}^{-1}$, except for rutile microspheres which had a very rough surface in contrast to anatase and amorphous titania microspheres. The particle-induced cell migration assay (PICMA; based on chemotaxis) of all titanium dioxide particles was comparable to the effect of control silica nanoparticles (50 nm, uncoated, agglomerated) but did not show a trend with respect to particle size, shape, or crystal structure. The coating with carboxymethylcellulose (CMC) had no significant biological effect. However, the rough surface of rutile microspheres clearly induced pro-inflammatory cell reactions that were not predictable by the primary particle size alone.

Keywords: titanium dioxide; titania; particles; inflammation; macrophages; particle-induced cell migration assay; rutile; anatase



Citation: Breisch, M.; Olejnik, M.; Loza, K.; Prymak, O.; Rosenkranz, N.; Bünger, J.; Sengstock, C.; Köller, M.; Westphal, G.; Eppler, M. Cell-Biological Response and Sub-Toxic Inflammatory Effects of Titanium Dioxide Particles with Defined Polymorphic Phase, Size, and Shape. *Nanomaterials* **2023**, *13*, 1621. <https://doi.org/10.3390/nano13101621>

Academic Editor: Jose L. Luque-Garcia

Received: 3 April 2023
Revised: 3 May 2023
Accepted: 10 May 2023
Published: 12 May 2023



Copyright: © 2023 by the authors. Licensee MDPI, Basel, Switzerland. This article is an open access article distributed under the terms and conditions of the Creative Commons Attribution (CC BY) license (<https://creativecommons.org/licenses/by/4.0/>).

1. Introduction

Titanium dioxide (TiO_2) occurs in three different polymorphic forms (tetragonal anatase, tetragonal rutile, and orthorhombic brookite), among which anatase and rutile have significant industrial importance. With an annual production of over 3 million tons, TiO_2 is one of the most important inorganic materials that has been used in many industrial applications for decades [1,2]. Its light-scattering properties caused by a very high refractive index and its semiconducting nature are the reasons for its application as white pigment in varnishes, paints, textiles, foods, and plastics [3,4]. TiO_2 is almost chemically inert, practically insoluble in aqueous solutions, and non-toxic. In addition, its main application as white pigment, micro- and nanoscale TiO_2 particles with very small diameters ($d < 100 \text{ nm}$) are also applied as UV absorber in sunscreens or as additive in food, toothpaste, and pharmaceuticals [5].

The International Agency for Research on Cancer (IARC) has classified titanium dioxide (TiO_2) as possibly carcinogenic to humans (Group 2B) on the basis of sufficient evidence

for carcinogenicity in animal experiments after inhalation. However, the human data were assessed as inadequate for classification [6]. According to German regulatory boards, TiO_2 is of rather low toxicity. Thus, the German workplace threshold limit (TLV) for granular particles without intrinsic toxicity (GBS) is partly based on TiO_2 toxicity data. This is based on the assumption that the carcinogenic effects of TiO_2 are caused by its inflammatory effects at chronic overload of the lung clearance and not by an inherent toxicity. In 2021, the European Union has banned the use of titanium dioxide as food additive (E171) due to health concerns (mainly genotoxicity) caused by ingested nanoparticles [7–10].

The risk assessment for TiO_2 is complicated by the fact that TiO_2 is used (and investigated) in different crystalline forms and with many different surface coatings—in particular when it is applied as a pigment in cosmetics, paints or printing inks. A TiO_2 mixture of 80% anatase and 20% rutile, which is also known as PM25, was mostly used for toxicological assessments [6]. Unfortunately, investigations of TiO_2 particles with defined crystallographic phase (polymorph) are rare, especially in the sub-toxic range.

Despite its extensive classification as a non-toxic substance, uncontrolled inhalative exposure to TiO_2 can be hazardous to humans [11–14]. This has been shown in a number of toxicological studies regarding possible hazards after inhalation [13–18]. However, toxicological data in systematic studies to assess TiO_2 particles depending on their polymorphic phase, their crystallinity, particle size, shape, coating and possible agglomeration behavior are not complete [10,12–14,19–22]. Commercially available TiO_2 nanoparticles, which usually consist of a rutile–anatase mixture, are often irregular, with a broad particle size distribution and significantly larger hydrodynamic size after redispersion in aqueous media, due to particle agglomeration [23]. This complicates the investigation of the inflammatory and toxicological effects with respect to the particle properties.

Our aim was to close this gap and to synthesize monodisperse and colloidally stable particles by sol-gel chemistry, which enables control over particle size, shape, and crystal form [24–27]. We pursued various synthetic routes to prepare particles with well-defined properties. Variation parameters were shape (spheres and rods), size (in length or diameter), and crystal structure (i.e., amorphous titania, crystalline anatase and crystalline rutile). Altogether, we prepared six types of TiO_2 particles. The particles were functionalized with anionic polyelectrolyte carboxymethyl cellulose (CMC) to obtain the same charge in all particle types and to prevent agglomeration and sedimentation as far as possible.

An in-depth cell-biological study with NR8383 macrophages at sub-toxic concentration to compare the effect of these chemically identical TiO_2 particles was performed to reveal the effect of these parameters on the production of inflammatory markers. The overall goal of this study was a statement as to whether size, shape, and crystal structure of granular bio-persistent dust should be taken into account when setting exposure limit values beyond current legal requirements.

2. Materials and Methods

2.1. Chemicals

We used titanium(IV)butoxide ($\text{Ti}(\text{OBu})_4$, Sigma-Aldrich, St. Louis, MO, USA; 97%), titanium(IV)iso-prop-oxide ($\text{Ti}(\text{O}^i\text{Pr})_4$, TTIP, Sigma-Aldrich, 97%), titanium tetrachloride (TiCl_4 , Sigma-Aldrich, 99.9%), carboxymethyl cellulose sodium salt (CMC, $M_W = 90,000 \text{ g mol}^{-1}$, Sigma-Aldrich), calcium chloride dihydrate ($\text{CaCl}_2 \cdot 2 \text{ H}_2\text{O}$, Sigma-Aldrich, >99%), methanol (Fisher Chemicals, Schwerte, Germany; p.a.), acetic acid (VWR Chemicals, Darmstadt, Germany, p.a., 99.7%), hydrochloric acid (VWR Chemicals, p.a., 37%), sulfuric acid (Roth, Karlsruhe, Germany; 96%), and potassium hydroxide (Sigma-Aldrich, 90%) as obtained. Ultrapure water was prepared with a Purelab ultra instrument (ELGA LabWater, Celle, Germany). All syntheses and characterizations were carried out with ultrapure water as solvent unless otherwise noted. Prior to the syntheses, all glassware was cleaned with concentrated sulfuric acid (140 °C, 30 min) and thoroughly washed with boiling water. Finally, all glassware was sterilized at 200 °C for 3 h.

2.2. Instruments

Dynamic light scattering for particle size analysis and zeta potential determination were carried out with a Malvern Zetasizer Nano ZS ZEN 3600 instrument (Malvern Panalytical Ltd., Malvern, UK; 25 °C, laser wavelength 633 nm; fixed angle 173°; backward scattering mode). A log-normal distribution was assumed as peak profile of the size distribution. The average particle diameter was represented as mean value of the maximum of the size distribution from the log-normal distribution fit. The polydispersity index (PDI) of the system was calculated from DLS measurements. The particles were dispersed in pure water at pH 7.

Ultraviolet-visible spectroscopy (UV/vis) was performed in Suprasil® micro quartz cuvettes with a Varian Cary 300 instrument (Agilent Technologies, Santa Clara, CA, USA). The solvent, as background correction, and the diluted particle dispersion were measured with sample volumes of 750 µL.

Fourier-transformed infrared spectroscopy (FT-IR) was performed by pressing the samples onto a diamond plate with an Attenuated Total Reflection (ATR) Alpha Platinum FT-IR instrument (Bruker, Billerica, MA, USA).

Combustion analysis was performed with an elemental analyzer EuroVector EA3000 (EuroVector, Pavia, Italy) to quantify the organic matter content in the samples (C, H in CMC).

For X-ray powder diffraction, particle powders that had been dried at 80 °C in air for 4 h were used. X-ray powder diffraction was carried out with a Bruker D8 Advance diffractometer operating in Bragg-Brentano geometry with Cu K α radiation ($\lambda = 1.54 \text{ \AA}$, 40 kV, and 40 mA). The samples were placed on single-crystalline silicon sample holders cut to a crystallographic (911) plane to minimize background scattering. The samples were analyzed from 5 to 90° 2 Θ with a step size of 0.01° and a counting time of 0.6 s at each step. The instrumental peak broadening was determined with lanthanum hexaboride as internal standard (LaB₆; NIST, National Institute of Standards and Technology; reference compound). Rietveld refinement was performed with the program package TOPAS 5.0 (Bruker) to determine lattice parameters and fractions of the different crystalline polymorphs of TiO₂. For the calculation of crystallite size, the Scherrer and Stokes-Wilson equations were used [28].

The diffraction pattern of both tetragonal phases of TiO₂ were taken from the ICDD database (International Centre for Diffraction Data) as reference (anatase: #21-1272, rutile #21-1276) and used for the qualitative phase analysis with Diffrac.Suite EVA V1.2 (Bruker).

Scanning electron microscopy was performed with an Apreo S LoVac instrument (Thermo Fisher Scientific, Waltham, MA, USA) in combination with a Thermo Scientific UltraDry silicon drift X-ray detector on gold/palladium-sputtered samples.

To analyze the cellular uptake of titanium dioxide particles by scanning electron microscopy, the NR8383 cells were rinsed twice with PBS and fixed with a glutaraldehyde solution (3.7% in PBS, Sigma-Aldrich) for 15 min at room temperature. Fixed cells on round glass microscopy slides (Sarstedt, Nümbrecht, Germany) were rinsed twice with PBS again, and then the cells were dehydrated with an ascending sequence of ethanol (20%, 40%, 60%, 80%, 96–98%, 5 min each). Prior to investigation, the samples were sputtered with gold/palladium coating.

2.3. Synthesis of TiO₂ Particles

Amorphous titanium dioxide microspheres were synthesized by a one-pot synthesis according to Han et al. [29]. In a 250 mL round-bottom flask, 200 µL of an aqueous solution of CaCl₂ (0.05 M) was added to 50 mL methanol. The mixture was stirred for 10 min. Afterwards, 850 µL of TTIP was added dropwise during 1 min and the solution was stirred for 4 h at room temperature. After the reaction was finished, the microspheres were collected by centrifugation (3500 rpm, 30 min, Heraeus Fresco 21 centrifuge Thermo Scientific) and redispersed in water by ultrasonication. After each centrifugation, the

supernatant was removed, and the particle pellet was redispersed in water using an ultrasonic bath and dried at 80 °C for 4 h in air.

For the synthesis of anatase microspheres we used the amorphous titanium dioxide microspheres. Dried titanium dioxide microspheres were transferred to a porcelain crucible, heated to 500 °C within one hour and held at that temperature for 1 h. The calcined particles were cooled down to room temperature and then redispersed in water by ultrasonication. The purification of the anatase microspheres was carried out in the same way as for the amorphous particles.

Anatase nanospheres were synthesized by a solvothermal method according to Ye et al. [30]. In a 50 mL centrifuge tube (Corning, NY, USA), 0.75 mL of $\text{Ti}(\text{OBu})_4$ was added dropwise to 15 mL acetic acid. After vigorous stirring at room temperature for 20 min, the complete solution was transferred into a 20 mL PTFE-lined autoclave, closed, and annealed at 200 °C for 24 h. After cooling down, the particle solution was collected by centrifugation (3500 rpm, 1 h). The particles were washed three times with water by the same centrifugation procedure and dried at 80 °C for 4 h in air.

The synthesis route for rutile nanorods was adapted and modified from Dong et al. [31]. In a 50 mL centrifuge tube (Corning), 10 mL of $\text{Ti}(\text{OBu})_4$ was rapidly added under vigorous stirring to an aqueous solution of HCl (30 mL, 3 M) at room temperature. After the complete addition of $\text{Ti}(\text{OBu})_4$, a solid was formed which completely dissolved within 2 h together with the formation of a two-phase system. After 2 h, the solution was stirred very slowly (50 rpm) for 16 h to allow the formation of the nanoparticles. The rutile nanorods were isolated by centrifugation (3500 rpm, 90 min), washed with water three times by the same centrifugation procedure and dried at 80 °C for 4 h on air.

Rutile sub-microrods were prepared according to Dong et al. [31], with modifications. In a 50 mL centrifuge tube (Corning®), 8.5 mL of $\text{Ti}(\text{OBu})_4$ was added to an aqueous solution of HCl (30 mL, 3 M). The solution was vigorously stirred for 4 h at room temperature. After the stirring was stopped, 15 mL of the aqueous, almost colorless solution (inorganic phase of the formed two-phase system) were carefully removed and transferred to a PTFE vessel for the subsequent hydrothermal treatment. The hydrothermal reaction was carried out in a 20 mL PTFE-lined autoclave at 200 °C for 2 h. After 2 h, the reaction mixture was cooled to room temperature. The purification of rutile sub-microrods was performed by triple centrifugation (3500 rpm, 60 min) and washing with water three times. Finally, the particles were dried at 80 °C for 4 h in air.

The synthesis of rutile microspheres was based on the work of Yan et al. [32] and carried out with some modifications. First, 30 mL water was added into 500 mL three-neck flask under argon and cooled to 0 °C with an ice bath. After 10 min, 3.2 mL of TiCl_4 was injected with a syringe through a septum in argon atmosphere. Within 20 min, the solution turned from white to almost colorless. Then, 30 mL of an aqueous solution of KOH (1 mol L^{-1} , pre-cooled to 0 °C) was added, followed after 5 min by 0.3 mL HCl (37%). After 10 min, 15 mL of the colorless solution was transferred into a 20 mL PTFE-lined autoclave and heated to 100 °C for 24 h. The cooled particle dispersion was purified by centrifugation (3500 rpm, 30 min) and washed with water after redispersion by ultrasonication. The purification steps were repeated 3 times, and finally the rutile microspheres were dried at 80 °C for 4 h in air.

All dried titanium dioxide particles were surface-coated with CMC. In a 50 mL centrifuge tube (Corning®), 50 mg of each TiO_2 type was dispersed in 30 mL water by ultrasonication for 5 min. Then, 10 mL of an aqueous CMC solution (25 g L^{-1}) was added, followed by vigorous stirring for 12 h at room temperature. To remove excess CMC, the particles were purified by triple centrifugation in water, as described above. Finally, the CMC-functionalized TiO_2 particles were dried at 80 °C for 4 h in air.

The number of particles in 1 g solid was computed from the average particle mass for spheres and rods by the following procedure:

$$m_{\text{sphere}} = \frac{4}{3} \pi r^3 \rho$$

$$m_{\text{rod}} = \pi r^2 L \rho$$

with r the particle radius and L the particle length, both obtained by SEM analysis (Table 1), and ρ the densities of rutile (4200 kg m^{-3}), anatase (3900 kg m^{-3}), and amorphous TiO_2 (3650 kg m^{-3}) [33,34]. The specific surface area of particles (expressed as $\text{m}^2 \text{ g}^{-1}$) was calculated as follows:

$$S_{\text{spheres}} = 4\pi r^2 N_{\text{particles in 1 g}}$$

$$S_{\text{rods}} = (2\pi r^2 + 2\pi rL) N_{\text{particles in 1 g}}$$

2.4. Particle Storage and Treatment

After synthesis, the TiO_2 particles were stored at 4°C in the dark under argon atmosphere. Stock solutions in sterile water were adjusted to a particle concentration of 4 mg mL^{-1} . Immediately before use in cell culture experiments, the particles were dispersed by ultrasonication (Elma Sonic S10, Elma Ultrasonic, Singen, Germany; 30 W, 5 min) and thorough vortexing. They were applied to the cells at the final concentrations in a well of 25, 50, 100, 200, and $300 \text{ }\mu\text{g mL}^{-1}$, respectively.

2.5. Cell Culture

To study the biological activity of the TiO_2 particles, the rat alveolar macrophage cell line NR8383 (LGC Standards GmbH, Wesel, Germany) was used. Cultivation of cells was carried out in Ham's F-12 medium with additional 15% fetal calf serum (FCS, GIBCO, Invitrogen, Karlsruhe, Germany) at standard cell culture conditions (humidified atmosphere, 37°C , 5% CO_2) in 175 cm^2 cell culture flasks (BD Falcon, Becton Dickinson GmbH, Heidelberg, Germany). The partly adherent NR8383 cells (1:1 ratio of adherent:non-adherent cells) were scraped from cell culture flasks with a cell scraper (TPP Techno Plastic Products AG, Trasadingen, Switzerland) and mixed with the non-adherent cell portion before seeding $2.4 \times 10^5 \text{ cells cm}^{-2}$ in 24-well cell culture plates (BD Falcon; Fisher Scientific).

2.6. Cytotoxicity Assay

The toxic effects of the different TiO_2 particles at various concentrations ($25\text{--}300 \text{ }\mu\text{g mL}^{-1}$) on NR8383 cells compared to unexposed control cells were evaluated by propidium iodide staining (PI, Sigma-Aldrich) of non-viable cells and flow cytometry. Briefly, after particle exposure for 2 h or 16 h, cells were collected as described above and transferred to 5 mL tubes (BD Biosciences). PI staining was performed with $50 \text{ }\mu\text{g mL}^{-1}$ PI for 10 min at RT in the dark. Subsequently, the fraction of non-viable (PI positive) cells was detected by flow cytometry (FACSCalibur, BD Bioscience, Heidelberg, Germany) and quantified with the CELLQuest 1.2.2 software (BD Biosciences). A total number of 15,000 cells was analyzed for each measurement (see Figure S1 for details).

2.7. Generation of Reactive Oxygen Species (ROS)

The intracellular generation of ROS in NR8383 cells upon incubation with the different TiO_2 particles ($25\text{--}300 \text{ }\mu\text{g mL}^{-1}$) was measured by the DCF assay. After 2 h of particle exposure, the cells were collected and treated with the cell-permeable ROS indicator 2',7'-dichlorodihydrofluorescein diacetate ($20 \text{ }\mu\text{M H}_2\text{DCFDA}$, Thermo Fisher Scientific, Waltham, USA) for 30 min at 37°C in the dark. In addition, the cells were incubated for 30 min with a hydrogen peroxide solution (3% H_2O_2 , Herbeta Arzneimittel, Berlin, Germany), which served as a positive control for enhanced ROS levels. The conversion of the non-fluorescent H_2DCFDA dye into the highly fluorescent 2',7'-dichlorofluorescein (DCF) form by generated ROS was quantified by flow cytometry (15,000 cells per measurement). Additional PI staining allowed for discrimination between viable and non-viable cells (see Figure S2 for details).

2.8. Protein Microarray

Microarray analysis was performed with supernatants of NR8383 cells after 16 h of exposure to $100 \mu\text{g mL}^{-1}$ of the different TiO_2 particles with a Proteome Profiler Rat XL Cytokine Array (Bio-Techne GmbH, Wiesbaden-Nordenstadt, Germany). This nitrocellulose membrane-based sandwich immuno-array allowed a semi-quantitative analysis of 79 different bioactive factors (e.g., cytokines, growth factors). The supernatants of particle-treated NR8383 cells were centrifuged at 300 g for 10 min and stored at -20°C . Subsequent microarray analysis was carried out according to the manufacturer's instructions. Briefly, supernatants were applied to the membranes, where captured antibodies, spotted as duplicated dots, bound the target proteins from the sample. The captured proteins were then detected with biotinylated detection antibodies, followed by visualization with chemiluminescent detection reagents. Detection and quantification of the chemiluminescence signals were performed with an Amersham Imager 600 RGB and the ImageQuantTL software (Amersham, GE Healthcare Bio Science, Uppsala, Sweden). According to the proteomic repertoire of NR8383 [35], 27 factors were considered for detailed review.

2.9. Particle Induced Cell Migration Assay (PICMA)

PICMA was performed as described earlier [23]. Briefly, NR8383 rat macrophages (LGC Standards, Wesel, Germany) were cultivated at 37°C , 100% humidity, and 5% CO_2 in Ham's F-12 + 15% FCS (PAN-Biotech GmbH, Aidenbach, Germany), 2 mM L-glutamine, $100 \mu\text{g mL}^{-1}$ penicillin, and 100 U mL^{-1} streptomycin (PAN-Biotech GmbH, Aidenbach, Germany). Approximately 3×10^6 cells were seeded in 25 mL (175 cm^2) medium.

We used trans-retinal differentiated HL-60 cells (dHL-60) for the investigation of chemotaxis. The HL-60 cells (DSMZ, Braunschweig, Germany) were differentiated in RPMI 1640 medium +10% FCS, 2 mM L-glutamine, $100 \mu\text{g mL}^{-1}$ penicillin, 100 U mL^{-1} streptomycin and $1 \mu\text{M}$ trans-retinoic acid (Sigma-Aldrich, Steinheim, Germany) for three days.

For particle incubation, 3×10^6 NR8383 cells mL^{-1} were seeded in 12.5 cm^2 cell culture flasks at a final volume of 3 mL (2.4×10^5 cells cm^{-2}). A sample in which cells without particles were incubated served as negative control. Incubation of the NR8383 cells with the particles was performed for 16 h. Thereafter, the cells were removed by centrifugation at 300 g for 5 min, and the particles were removed by centrifugation with 15,000 g for 10 min at room temperature.

Cell migration was investigated as introduced by Boyden [36], with modifications described by Westphal et al. [37]. Briefly, 200,000 dHL-60 cells were cultured in 200 μL RPMI 1640 medium without FCS and seeded in each plate. A well insert (THINCERT, $3 \mu\text{m}$ pore size, Greiner bio-one, Frickenhausen, Germany) was put into the cavities of black 24-well plates (Krystal, Dunn Labortechnik, Asbach, Germany) and then 500 μL of the supernatants of the NR8383 cells treated with TiO_2 particles were added to the lower chamber. Migration of dHL-60 cells was performed for 24 h. 0 to 100,000 HL-60 cells were seeded directly into four-well plates that were left without inserts for calibration. Migrated cells and calibration cells were stained with calcein (Sigma-Aldrich). The cell count was determined by fluorescence spectroscopy at 490/520 nm (SpectraMax M3, Molecular Devices, Sunnyvale, CA, USA). As reference, we used uncoated silica nano particles (CAS No. 7631-86-9, Lot MKBF2889V, 99.5%, 10–20 nm) (Sigma-Aldrich) [23].

2.10. Statistical Analysis

Data are expressed as the mean \pm SD and given as the percentage of the control (cells not exposed to particles). For statistical evaluation, one-way analysis of variance (ANOVA) with Dunett's Multiple Comparison Test was applied with the GraphPad Prism software (GraphPad Software Inc., San Diego, CA, USA). p values ≤ 0.05 were considered as statistically significant.

3. Results

Six different types of titanium dioxide particles with defined shape (spheres, rods), particle size, and crystal structure (anatase, rutile or amorphous), all both unfunctionalized (“naked”) and CMC-coated, were wet-chemically prepared. The particles were comprehensively characterized by different analytical methods, i.e., scanning electron microscopy (SEM), dynamic light scattering (DLS), UV/vis spectroscopy, infrared (IR) spectroscopy, X-ray powder diffraction (XRD), and elemental analysis (EA). All characterization results are summarized in Table 1. The content of CMC is approximately two times the carbon content (as carbon could also come from impurities), i.e., the particles contained between 1 and 5 wt% CMC.

Particle size and shape of all titanium dioxide particles were determined by SEM. Scanning electron micrographs showed that the control of the particle shape (spherical or rod-shaped) and the control of the particle size in three ranges (“nano”, “sub-micro”, “micro”) were made possible by variation of the reaction parameters. Another challenge was the control of the polymorphic phase, i.e., anatase or rutile. Figure 1 shows scanning electron micrographs of all particles. There was no difference between unfunctionalized and CMC-coated particles, except for very high-resolution images, where the polymer led to a slightly blurred particle surface.

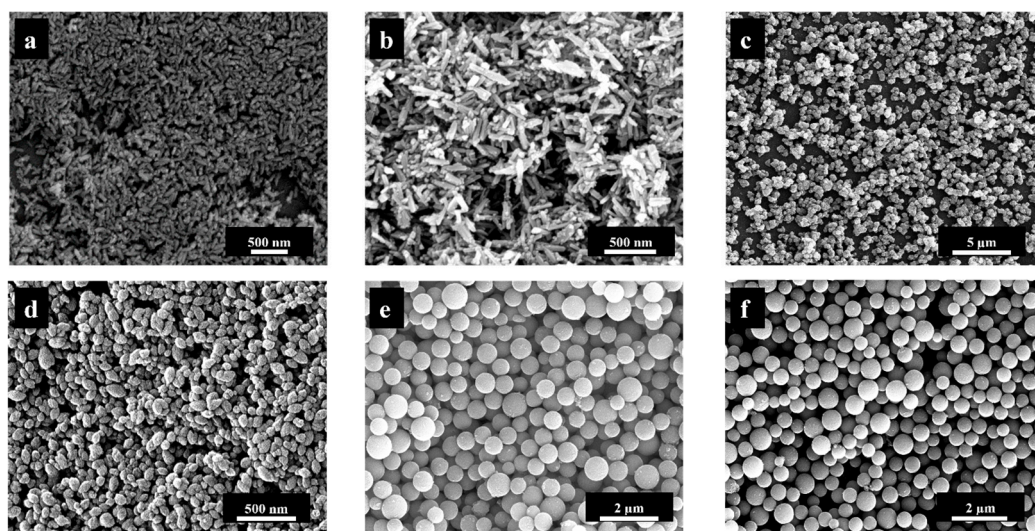


Figure 1. Representative SEM images of unfunctionalized titanium dioxide particles: Rutile nanorods (a), rutile sub-microrods (b), rutile microspheres (c), anatase nanospheres (d), amorphous titania microspheres (e), and anatase microspheres (f).

As can be seen in Figure 2, the anatase microspheres consisted of spherical crystallites and had a very smooth surface, while the rutile microspheres were significantly rougher. This is visible on the particle surface, which consisted of stacked nanorods. The surface of the amorphous titania microspheres was also very smooth (see Figure 1e).

Dynamic light scattering (DLS) was used to investigate the colloidal stability and the particle size distribution in aqueous dispersion (Figure 3). In all cases the polydispersity index (PDI) was below 0.3, which indicated a good dispersibility. The dispersed particles were not strongly agglomerated, as the comparison between the diameters by SEM and by DLS indicates (Table 1).

The zeta potential was also determined by dynamic light scattering. Due to the presence of Ti-OH groups on the particle surface, the unfunctionalized TiO₂ particles were electrostatically stabilized, as indicated by the zeta potential. The coating of the particles with the anionic polyelectrolyte carboxymethylcellulose (CMC) led to charge reversal and an electro-steric stabilization.

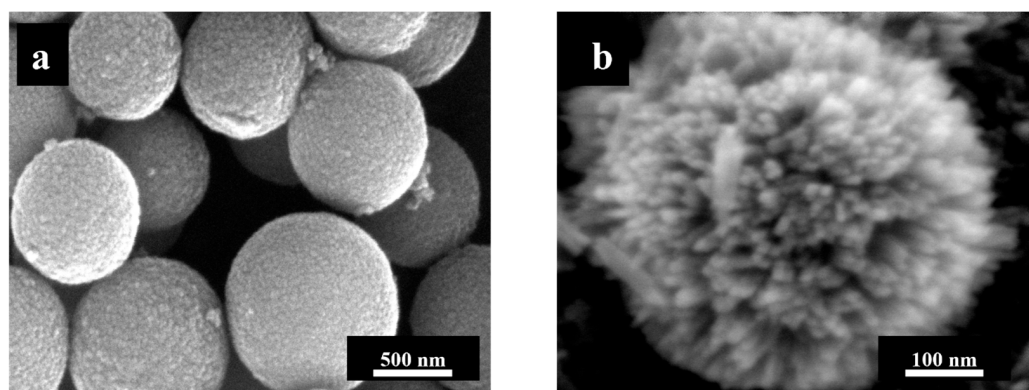


Figure 2. High-resolution SEM images of the surface of unfunctionalized titanium dioxide particles: Anatase microspheres (a) and rutile microspheres (b).

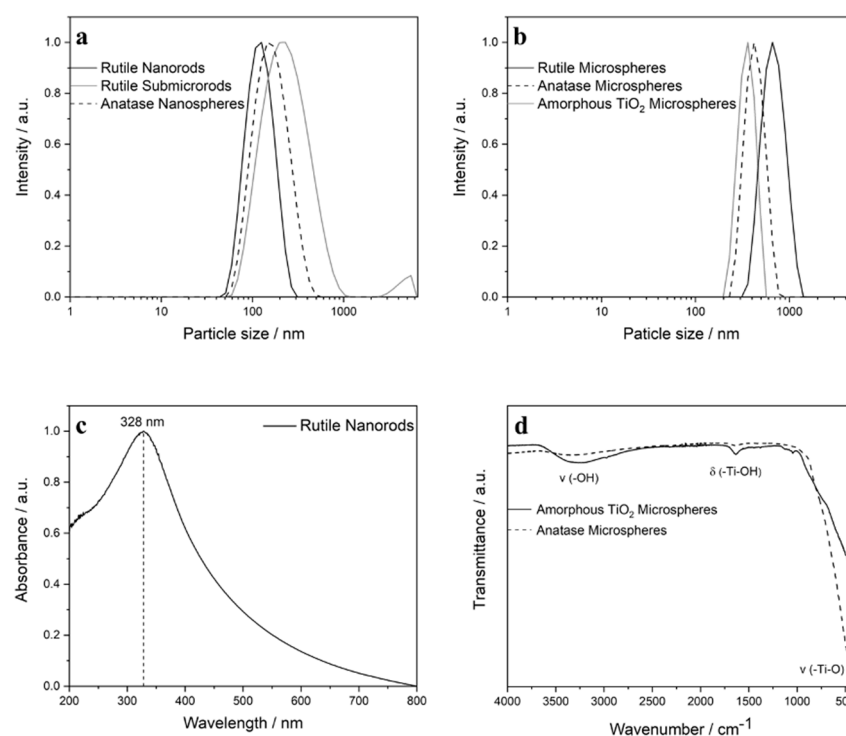


Figure 3. Representative characterization data of unfunctionalized TiO_2 particles: DLS data of TiO_2 nano- and sub-micro particles (a), DLS data of TiO_2 microparticles (b), UV/vis spectroscopy of rutile nanorods (c), and IR spectroscopy of amorphous titania microspheres before calcination and anatase microspheres after calcination (d). The other particle shapes gave similar results.

In addition to the zeta potential measurements, the particles were analyzed by IR spectroscopy (Figure 3). IR spectra of amorphous microspheres and anatase microspheres showed characteristic vibrations of Ti-O-Ti bonds at 403 cm^{-1} and of Ti-OH groups at 1636 cm^{-1} [38], whose intensity decreased after calcination due to condensation under release of water (additional IR spectra are shown in Figures S12–S17). UV-vis spectroscopy provided information about the optical properties of the particles (Figure 3). As expected, only the rutile nanorods gave a near-UV absorption peak at 328 nm [39]. Additional UV spectra are shown in Figures S18–S21.

Table 1. Physicochemical characterization data of unfunctionalized and CMC-coated TiO₂ particles. Standard deviation of the last digits given in parentheses.

	Size by SEM/nm	Size by DLS/nm	PDI from DLS	Zeta Potential by DLS/mV	Size by DLS/nm	PDI from DLS	Zeta Potential by DLS/mV	Carbon Content by EA/wt%
	Unfunctionalized ("Naked")				CMC-Coated			
Rutile particles								
Nanorods	70 (20) × 25 (6)	106	0.12	+38	233	0.23	−17	1.8
Sub-microrods	190 (60) × 40 (10)	207	0.24	+25	209	0.27	−24	0.5
Microspheres	620 (160)	509	0.19	+23	650	0.38	−6	0.4
Anatase particles								
Nanospheres	100 (21)	143	0.05	+33	161	0.14	−20	0.6
Microspheres	510 (89)	618	0.05	+23	574	0.11	−29	1.5
Amorphous particles								
Microspheres	620 (101)	649	0.10	−25	705	0.03	−29	2.5

The TiO₂ samples were examined by X-ray powder diffraction to assess their crystal structure, followed by quantitative Rietveld refinement (Figure 4 and Table 2). TiO₂ microspheres prepared from titanium alcoholates by sol-gel chemistry were fully X-ray amorphous. The phase transition from amorphous to crystalline during the calcination step led to the formation of pure anatase. Anatase nanospheres, rutile nanorods, and rutile sub-microrods were phase-pure, probably determined by the type of acid used during the synthesis. The rutile sub-microrods contained a small impurity of anatase. The Rietveld refinement data of the crystalline TiO₂ particles agreed well with the literature data for both polymorphs, i.e., anatase (tetragonal, space group $I4_1/amd$ with $a = 3.785 \text{ \AA}$ and $c = 9.514 \text{ \AA}$) and rutile (tetragonal, space group $P4_2/mnm$ with $a = 4.593 \text{ \AA}$ and $c = 2.959 \text{ \AA}$). The mean crystallite size of all crystalline particles from Rietveld refinement was smaller than the particle size observed by SEM (see Table 1), indicating a polycrystalline nature of all particles. In other words, each particle shown in SEM consists of a number of smaller crystallites, i.e., it is not a single crystal.

Table 2. X-ray powder diffraction data of crystalline TiO₂ particles (unfunctionalized) by Rietveld refinement. a and c lattice parameters of the tetragonal unit cell; ρ X-ray density; CS crystallite size. *: The rutile sub-microrods contained 96.4 wt% rutile and 3.6 wt% anatase.

	Rutile Nanorods	Rutile Sub-Microrods *	Rutile Microspheres	Anatase Nanospheres	Anatase Microspheres
$a/\text{\AA}$	4.620 (1)	4.605 (1)	4.610 (6)	3.794 (3)	3.791 (3)
$c/\text{\AA}$	2.960 (2)	2.963 (2)	2.959 (4)	9.514 (7)	9.507 (8)
$\rho/\text{g cm}^{-3}$	4.19	4.22	4.22	3.87	3.88
CS/nm	6.2 (1)	25 (1)	10.3 (10)	11.5 (10)	15 (1)

Particle precipitation and diffusion in cell culture medium depend on particle size, agglomeration state, density, and surface coating. This can significantly affect the dose which an adherent cell experiences at the bottom of a cell culture dish. For that reason, we have estimated the particle transport in water and in cell culture media (DMEM supplemented with 10% FCS) by simultaneous solution of the Stokes-Einstein equation and Stokes Law, with the in vitro sedimentation, diffusion and dosimetry model (ISDD) [40–42]. Figure 5 shows precipitation and diffusion rates of TiO₂ particles according to the ISDD model in water and in cell culture medium. The fast precipitation of TiO₂ microspheres is due to sedimentation, whereas the slower transport of nanoparticles is affected by diffusion and sedimentation. There was no significant difference between water and cell culture medium as dispersion medium.

The uptake of TiO₂ particles by NR8383 cells after 24 h was assessed by backscattered electron (BSE) imaging in a scanning electron microscope, taking advantage of the dependence of the contrast from the atomic number Z . Titanium (atomic number $Z = 22$) appears brighter in a BSE image compared to lighter elements, such as carbon (atomic

number $Z = 6$), nitrogen (atomic number $Z = 7$), or oxygen (atomic number $Z = 8$). All particles were strongly taken up by the cells, irrespective of their size, shape or CMC coating, well in line with general observations of the interaction of nanoparticles [43–47] and microparticles [47–50] with cells (Figure 6).

Energy-dispersive X-ray spectroscopy (EDS) was performed to confirm the particle uptake by NR8383 macrophages and the particle identity. Figure 7 shows representative EDS elemental mapping for untreated cells and after incubation with anatase microspheres. The SEM and EDS images clearly demonstrate that all types of TiO_2 particles were taken up well by the cells. However, a quantitative evaluation of the uptake is not possible from these data.

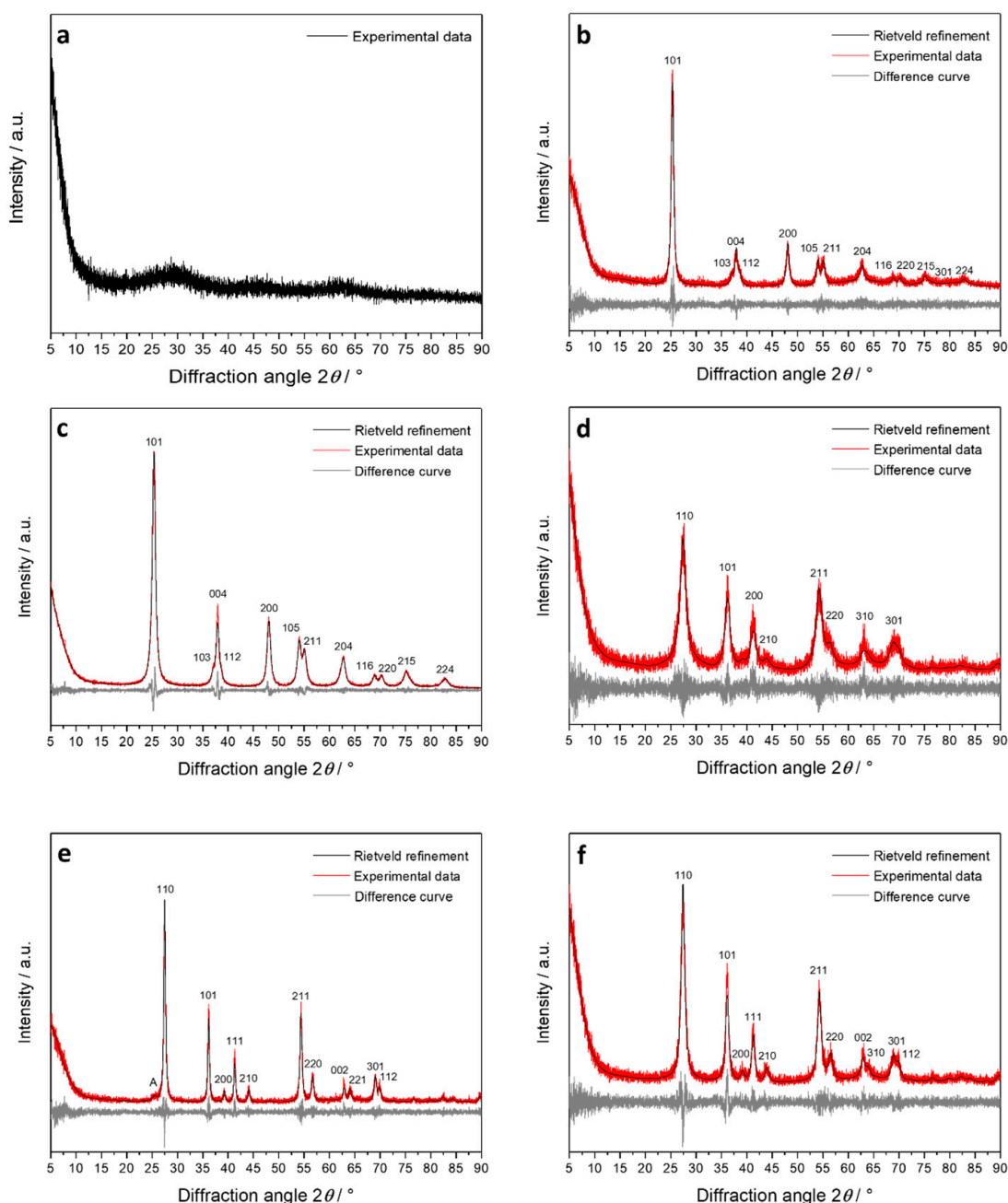


Figure 4. X-ray powder diffractograms of TiO_2 particles: Amorphous titania microspheres (a), anatase microspheres (b), anatase nanospheres (c), rutile nanorods (d), rutile sub-microrods, containing a small amount of anatase (A) (e), and rutile microspheres (f).

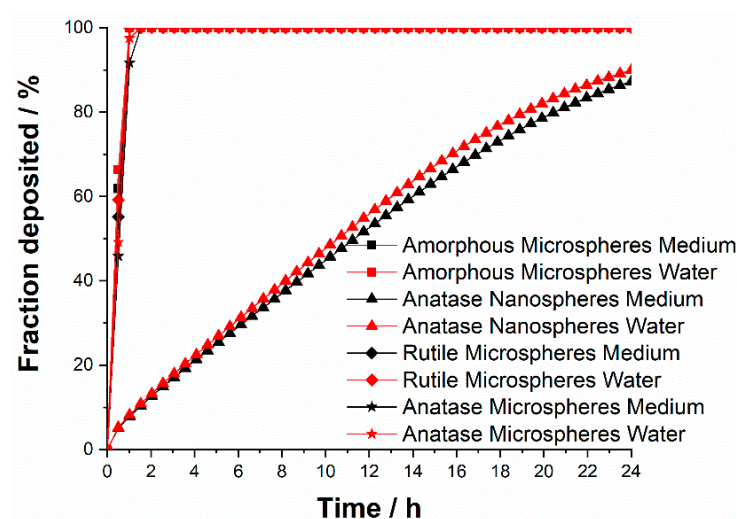


Figure 5. Precipitation and diffusion of TiO_2 particles according to the ISDD model [42] in water and in cell culture medium (DMEM supplemented with 10% FCS).

Potential cytotoxic effects of the different TiO_2 particles on NR8383 alveolar macrophages were determined by flow cytometric analysis of PI-labeled, non-viable cells after 2 h and 16 h of incubation (Figure 8). After 2 h of incubation, all rutile particles (nanorods, sub-microrods, microspheres) and anatase nanospheres induced a significant cytotoxicity compared to non-treated control cells, although only at high particle concentrations of $\geq 100 \mu\text{g mL}^{-1}$. For all types of TiO_2 particles, the cell toxicity increased with prolonged incubation time, which was reflected by the increased number of PI-positive cells. However, even after 16 h of exposure, none of the particles exhibited significant effects on the cell viability at concentrations below $100 \mu\text{g mL}^{-1}$. Among all tested particles, rutile microspheres had the highest cytotoxic activity, which was possibly caused by the rough particle surface consisting of stacked nanorods (see Figure 2b). The CMC-coating had no statistically significant effect on the biological activity of anatase and amorphous spheres, but in the case of rutile particles, most apparently for microspheres, unfunctionalized particles were less toxic than CMC-functionalized ones.

The formation of reactive oxygen species (ROS) in NR8383 macrophages after 2 h of incubation with the different TiO_2 particles was examined by the DCF assay and flow cytometry (Figure 9). Compared to non-treated control cells, NR8383 cells exposed to 200 and $300 \mu\text{g mL}^{-1}$ rutile nano- and sub-microrods caused significantly enhanced ROS levels, while, in the presence of the spherical particles, only a minor effect on ROS generation was detected. Overall, at moderate particle concentrations, none of the TiO_2 particles provoked cell activation associated with elevated ROS.

To further analyze possible cell-activating effects of the TiO_2 particles, the expression of bioactive factors was detected from NR8383 cell supernatants after 16 h of exposure to $100 \mu\text{g mL}^{-1}$ of the different particles. 79 bioactive molecules, including cytokines, chemokines, and growth factors, were detected simultaneously from each cell supernatant sample with a protein microarray. According to the proteomic repertoire of the NR8383 cell line [35], 27 factors were selected for a detailed view and are presented in the qualitative heat map in Figure 10.

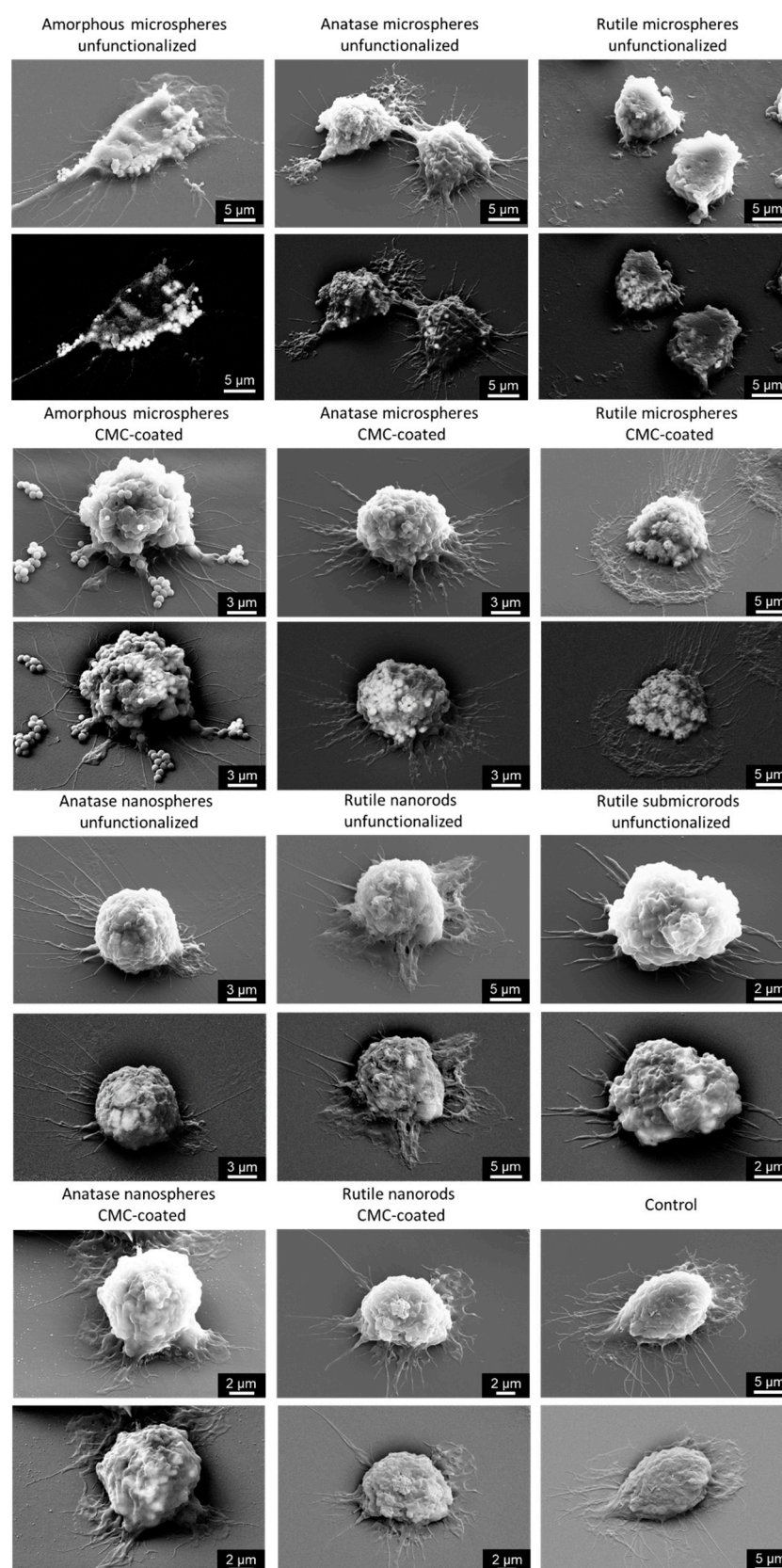


Figure 6. Representative scanning electron micrographs of NR8383 cells after 24 h of incubation with $50 \mu\text{g mL}^{-1}$ TiO_2 particles with secondary electron detector (top image for each sample) and backscattering electron detector (bottom image for each sample).

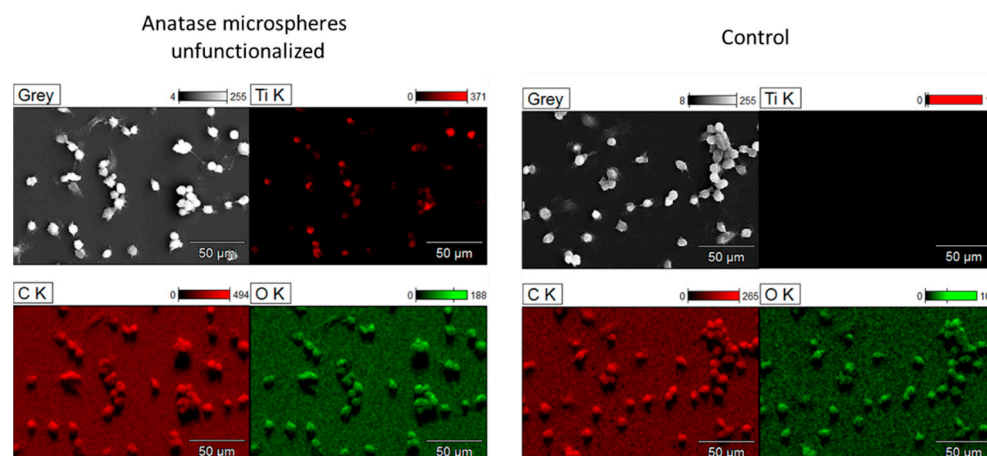


Figure 7. EDS elemental mapping of NR8383 macrophages after incubation with TiO_2 particles for 24 h (unfunctionalized anatase microspheres; **left**) and untreated cells for comparison (**right**). EDS data of the other particle types can be found in Figures S3–S11.

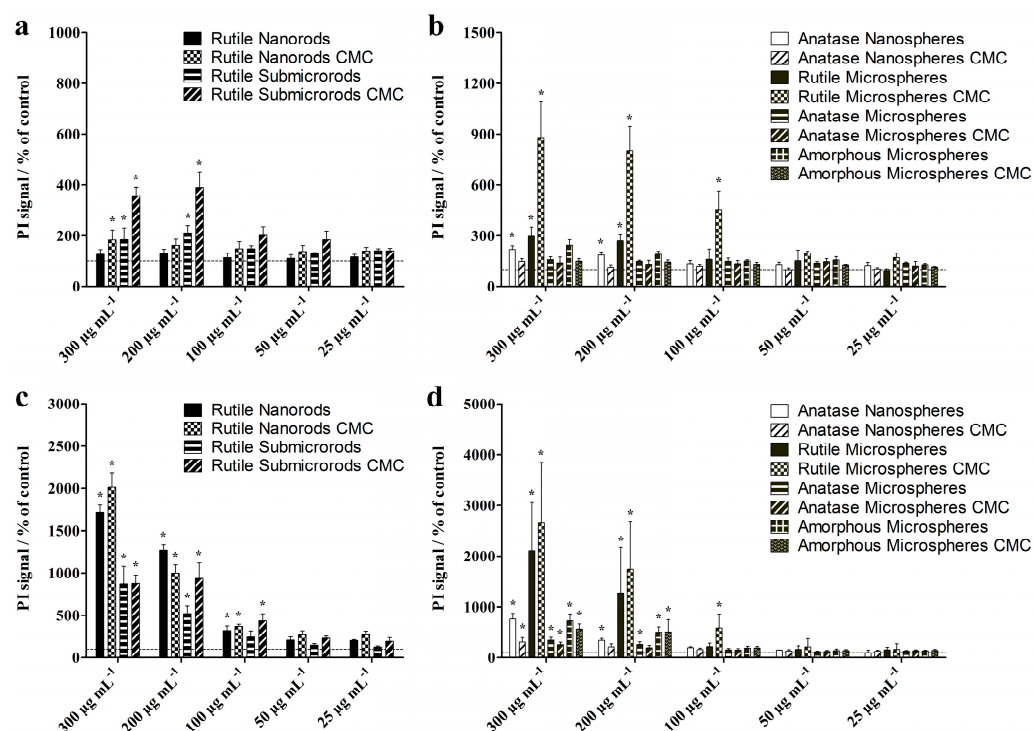


Figure 8. Toxic effects on NR8383 alveolar macrophages after 2 h (**a,b**) and 16 h (**c,d**) of exposure to TiO_2 rods (**a,c**) and TiO_2 spheres (**b,d**) at different concentrations. The cell viability was assessed by staining of non-viable cells with PI and flow cytometric analysis of the mean PI fluorescence intensity. Data are expressed as mean \pm SD ($n = 3$), given as percentage of control (100%, non-treated cells). Asterisks (*) indicate significant differences in comparison to the control ($p \leq 0.05$).

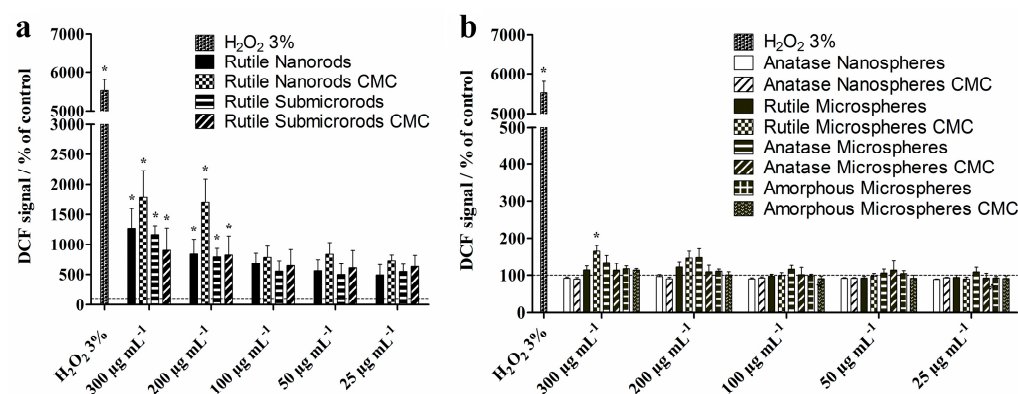


Figure 9. ROS levels in NR8383 alveolar macrophages after 2 h of exposure to TiO₂ rods (a) and TiO₂ spheres (b) at different concentration. Generation of ROS was determined by flow cytometric analysis of the mean fluorescence intensity of dichloro-fluorescein (DCF). A 3% H₂O₂ solution served as positive control for elevated ROS levels. Data are expressed as mean \pm SD ($n = 3$), given as the percentage of control (100%, non-treated cells). Asterisks (*) indicate significant differences in comparison to the control (* $p \leq 0.05$).

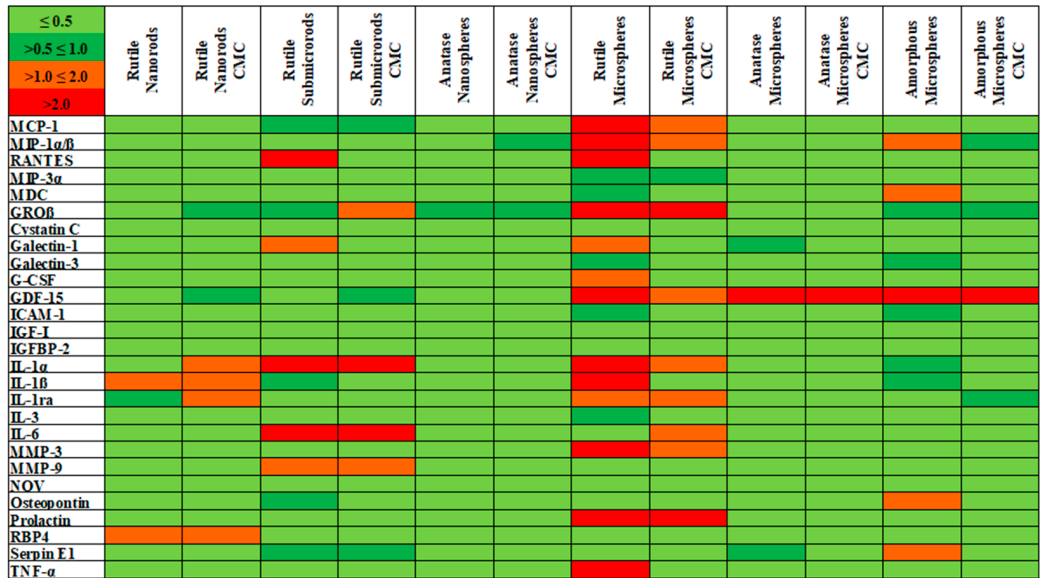


Figure 10. Heat map of selected bioactive factors expressed by NR8383 alveolar macrophages after 16 h of exposure to different TiO₂ particles (100 $\mu\text{g mL}^{-1}$). The expression of 27 factors, selected according to the proteomic NR8383 repertoire, was identified by a protein microarray. The standardized expression of the individual factors is presented relative to the control (i.e., no particle exposure) and encoded by the color intensity scale in the upper left corner (green for low expression, red for high expression).

An increase in the relative expression levels of the selected bioactive factors was observed for rutile sub-microrods, and this was even stronger for rutile microspheres, as indicated by an overall higher red content in the heat map. Rutile nanorods and anatase and amorphous spheres, by contrast, showed a higher green content, which indicated a reduced expression. Furthermore, an increased expression of GDF-15 was detected for all microspheres. GDF-15 expression was also observed earlier after challenge of NR8383 cells with asbestos fibers and multiwalled carbon nanotubes (MWCNT) [37]. It should be noted that the protein array analysis represents a qualitative screening method that provides a first overall impression of possible increase/decrease in expression patterns. However, a subsequent quantitative ELISA analysis revealed no statistically significant size-, morphology-, or structure-related effects and, therefore, no cell activation for the

examined TiO₂ particles. This confirms that the exposure to all TiO₂ particles was in the sub-toxic region.

Following our approach to elucidating the pro-inflammatory potential at sub-toxic concentrations, the attraction of dHL60 cells by supernatants from particle-treated NR8383 cells was investigated in the examined particles as an in vitro estimate for neutrophilic inflammation (Figure 11). The effects of all TiO₂ particles were smaller compared to the silica positive control. The TiO₂ curves were scattered around that of amorphous TiO₂, which showed a linear slope. Rutile nanorods showed the steepest slope and a hyperbolic course, whereas rutile microspheres exhibited the highest peak but a sigmoidal curve shape. Anatase micro- and nanospheres showed the weakest effects and nearly linear courses. Thus, the different TiO₂ particles caused different cell migration effects that were below the effect of the silica control particles (positive control; 50 nm, strongly agglomerated [23]) but not correlated with specific particle characteristics.

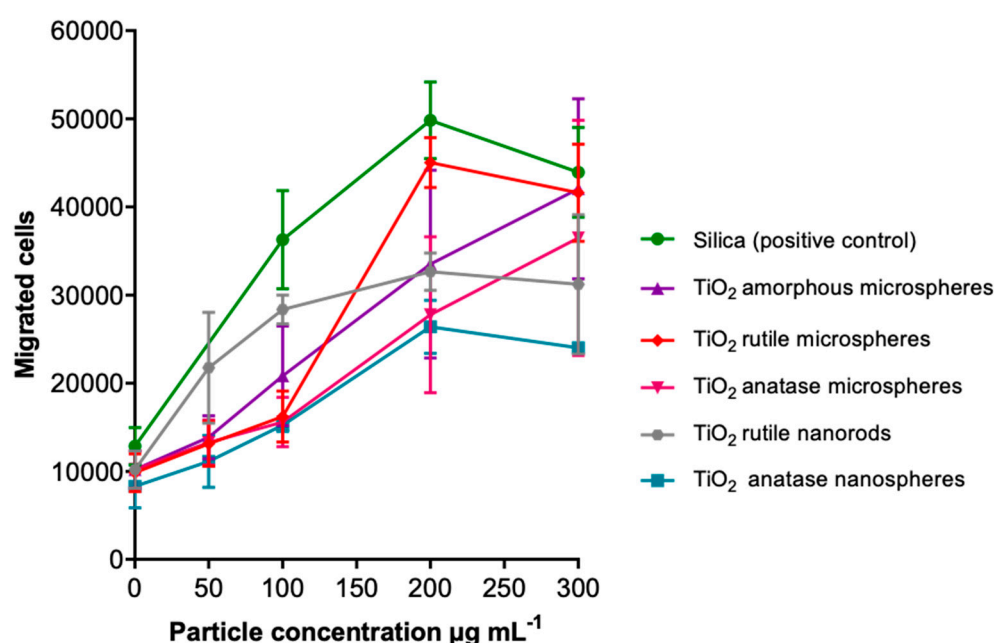


Figure 11. PICMA assay: Chemotaxis (migrated cells) of the unexposed dHL-60 cells in response to NR8383 cell supernatants that were obtained from incubation with TiO₂ particle concentrations between 50 and 300 µg mL^{−1}. Data are expressed as mean ± SD (*n* = 3). Commercial silica nanoparticles served as positive control.

Table 3 summarizes the particle concentration data at the subtoxic concentration of 100 µg mL^{−1}. Wiemann et al. [51] have defined a threshold of 4000 µm² particle surface area per cell for a non-toxic interaction with cells. As we are in all cases at or above this limit at a dose of 100 µg mL^{−1}, we can conclude that the effect of the particles was not due to a specific cytotoxicity but rather to an unspecific overload of the cells by non-soluble and inherently non-toxic particles. This confirms the observation that TiO₂ particles do not have an inherent toxicity.

Rutile microspheres had a particularly rough surface (Figure 2), i.e., the actual surface area was much higher than assessed by the particle geometry, which may explain its comparatively high pro-inflammatory activity. This is corroborated by the fact that anatase and titania microspheres of the same shape and almost the same size, but with a smooth surface, did not induce adverse reactions to cells.

We have earlier reported PICMA results for barium sulphate particles [52], for silica particles [53], for silica fibers [54], and for zinc oxide particles [55], all recorded in the sub-toxic range. The results reported here are in good agreement with these findings and confirm the suitability of PICMA to assess the pro-inflammatory effect of micro- and

nanoparticles. Barium sulfate as insoluble and bioinert material did not induce cell migration or proinflammatory effects [52]. Silica nanoparticles of different size and shape [53] and silica microrods [54] all had a low pro-inflammatory potential, possibly due to a hydrated surface in comparison to strongly pro-inflammatory quartz [23]. Zinc oxide as partially soluble material had a moderate pro-inflammatory effect that was attributed to the release of zinc ions [55]. Thus, PICMA is able to predict pro-inflammatory effects for particles at the sub-toxic level. This is important for its application as a rapid test for particles on the nano- and on the microscale. Clearly, the assessment of the acute toxicity is not sufficient to elucidate the inflammatory potential associated with particles of all kinds. The results presented here for titanium dioxide as one of the most prominent and most intensely discussed nano-material clearly underscore this fact.

Table 3. Concentration and dose data for all cell culture studies with TiO₂ particles (100 µg mL^{−1}) in a 24-well plate (2 cm², 640 µL, 48,000 cells). As the cytotoxic effects of particles are related to their total surface area, and also with respect to the number of cells, the data were converted to different ratios (see discussion). The particle numbers and the specific surface area were computed from the SEM particle size data.

	TiO ₂ Concentration/mmol L ^{−1}	TiO ₂ Particle Concentration/L ^{−1}	TiO ₂ Particle Surface Area/µm ² Per Particle	Total TiO ₂ Particle Surface Area/µm ² L ^{−1}	Total TiO ₂ Particle Surface Area Per Well/µm ²	Total TiO ₂ Particle Surface Area Per Cell/µm ²
Rutile nanorods	1.25	6.74×10^{14}	6.15×10^{-3}	4.1×10^{12}	2.6×10^9	55,200
Rutile sub-microrods	1.25	1.07×10^{14}	0.241	2.6×10^{12}	1.6×10^9	34,300
Rutile microspheres	1.25	1.93×10^{11}	1.20	0.2×10^{12}	1.5×10^8	3100
Anatase nanospheres	1.25	4.90×10^{13}	3.14×10^{-2}	1.5×10^{12}	1.0×10^9	21,000
Anatase microspheres	1.25	3.61×10^{11}	0.83	0.3×10^{12}	1.9×10^8	4000
Amorphous microspheres	1.25	2.21×10^{11}	1.20	0.3×10^{12}	1.7×10^8	3500

4. Conclusions

The in-vitro cell culture investigations showed no influence of size, shape, and crystal structure of chemically identical, granular TiO₂ particles on the investigated biological effects. Similar small differences of the biological effects that were not linked to distinct particle characteristics were earlier observed for zinc oxide particles [55] and silica particles [53]. Neither the particle-induced cell migration assay (PICMA), the cell toxicity, apoptosis, the release of signaling molecules, nor the formation of ROS showed effects that were correlated with the particle characteristics. The only major exception was the rough surface of rutile microspheres which—in contrast to the smooth surface of anatase microspheres and amorphous titania microspheres—induced pro-inflammatory effects. The dispersion state of the particles and their charge as changed by the application of a shell of carboxymethylcellulose (CMC) did not influence the cell-biological results. Taken together, these results suggest that shape and size of granular bio-persistent dust do not need to be considered for the setting of exposure limit beyond current regulatory provisions. However, comparative studies on other granular particles are desirable to elucidate whether these results can be generalized beyond titania.

Supplementary Materials: The following supporting information can be downloaded at: <https://www.mdpi.com/article/10.3390/nano13101621/s1>. In the supplementary data, IR and UV spectra of all particles, further EDS maps, and gating procedures for the analysis of flow cytometry data can be found. Figure S1: Gating strategy for the detection of non-viable NR8383 cells by flow cytometric analysis using the example of unexposed cell control (a), rutile nanorods (b) und CMC-functionalized rutil nanorods (c). Figure S2: Gating strategy for the detection of generated ROS in NR8383 cells by flow cytometric analysis using the example of cells exposed to 3% H₂O₂ for 2 h. Figure S3: EDS elemental mapping of NR8383 macrophages after incubation with CMC-functionalized anatase microspheres for 24 h. Figure S4: EDS elemental mapping of NR8383 macrophages after incubation with unfunctionalized anatase nanospheres for 24 h. Figure S5: EDS elemental mapping of NR8383

macrophages after incubation with CMC-functionalized anatase nanospheres for 24 h. Figure S6: EDS elemental mapping of NR8383 macrophages after incubation with unfunctionalized rutile microspheres for 24 h. Figure S7: EDS elemental mapping of NR8383 macrophages after incubation with CMC-functionalized rutile microspheres for 24 h. Figure S8: EDS elemental mapping of NR8383 macrophages after incubation with unfunctionalized rutile submicrorods for 24 h. Figure S9: EDS elemental mapping of NR8383 macrophages after incubation with CMC-functionalized rutile submicrorods for 24 h. Figure S10: EDS elemental mapping of NR8383 macrophages after incubation with unfunctionalized rutile nanorods for 24 h. Figure S11: EDS elemental mapping of NR8383 macrophages after incubation with CMC-functionalized rutile nanorods for 24 h. Figure S12: IR spectrum of amorphous TiO₂ microspheres. Figure S13: IR spectrum of anatase microspheres. Figure S14: IR spectrum of anatase nanospheres. Figure S15: IR spectrum of rutile nanorods. Figure S16: IR spectrum of rutile submicrorods. Figure S17: IR spectrum of rutile microrods. Figure S18: UV/vis spectrum of amorphous TiO₂ microspheres. Figure S19: UV/vis spectrum of anatase nanospheres. Figure S20: UV/vis spectrum of rutile nanorods. Figure S21: UV/vis spectrum of rutile submicrorods.

Author Contributions: Conceptualization J.B., C.S., M.K., G.W. and M.E.; methodology all authors; validation all authors; formal analysis all authors; investigation M.B., M.O., K.L., O.P. and N.R.; resources J.B., C.S., M.K., G.W. and M.E.; data curation all authors; writing—original draft preparation, all authors; writing—review and editing all authors; visualization M.B., M.O., K.L., O.P. and N.R.; supervision J.B., C.S., M.K., G.W. and M.E.; project administration J.B., C.S., M.K., G.W. and M.E.; funding acquisition J.B., C.S., M.K., G.W. and M.E. All authors have read and agreed to the published version of the manuscript.

Funding: This research was funded by Deutsche Gesetzliche Unfallversicherung (DGUV, projects FP 412 and FP 474).

Data Availability Statement: The data presented in this study are available on request from the corresponding author.

Conflicts of Interest: The authors declare no conflict of interest.

References

1. Ullattil, S.; Periyat, P. Sol-gel synthesis of titanium dioxide. In *Sol-Gel Materials for Energy, Environment and Electronic Applications, Advances in Sol-Gel Derived Materials and Technologie*; Pillai, S.C., Hehir, S., Eds.; Springer: Berlin/Heidelberg, Germany, 2017; pp. 271–283.
2. Dransfield, G.P. Inorganic sunscreens. *Radiat. Prot. Dosim.* **2000**, *91*, 271–273. [CrossRef]
3. Chen, X.; Mao, S.S. Titanium dioxide nanomaterials: Synthesis, properties, modifications, and applications. *Chem. Rev.* **2007**, *107*, 2891–2959. [CrossRef] [PubMed]
4. Braun, J.H.; Baidins, A.; Marganski, R.E. TiO₂ pigment technology: A review. *Prog. Org. Coat.* **1992**, *20*, 105–138. [CrossRef]
5. Fisher, J.; Egerton, T.A. Titanium Compounds, Inorganic. In *Kirk-Othmer Encyclopedia of Chemical Technology*; John Wiley and Sons: Hoboken, NJ, USA, 2001.
6. Baan, R.A. Carcinogenic hazards from inhaled carbon black, titanium dioxide, and talc not containing asbestos or asbestiform fibers: Recent evaluations by an IARC Monographs working group. *Inhal. Toxicol.* **2007**, *19*, 213–228. [CrossRef] [PubMed]
7. European Food Safety Authority (EFSA). Food Safety: Food Additive Titanium Dioxide Banned as of this Summer. 2022. Available online: https://cyprus.representation.ec.europa.eu/news/food-safety-food-additive-titanium-dioxide-banned-summer-2022-01-14_en (accessed on 22 March 2023).
8. European Commission. Titanium Dioxide: E171 No Longer Considered Safe When Used as a Food Additive. 2021. Available online: <https://www.efsa.europa.eu/en/news/titanium-dioxide-e171-no-longer-considered-safe-when-used-food-additive> (accessed on 22 March 2023).
9. Winkler, H.C.; Notter, T.; Meyer, U.; Naegeli, H. Critical review of the safety assessment of titanium dioxide additives in food. *J. Nanobiotechnol.* **2018**, *16*, 51. [CrossRef] [PubMed]
10. da Silva, A.B.; Miniter, M.; Thom, W.; Hewitt, R.E.; Wills, J.; Jugdaohsingh, R.; Powell, J.J. Gastrointestinal absorption and toxicity of nanoparticles and microparticles: Myth, reality and pitfalls explored through titanium dioxide. *Curr. Opin. Toxicol.* **2020**, *19*, 112–120. [CrossRef]
11. Skocaj, M.; Filipic, M.; Petkovic, J.; Novak, S. Titanium dioxide in our everyday life; Is it safe? *Radiat. Oncol.* **2011**, *45*, 227–247. [CrossRef]
12. Chen, Q.R.; Riviere, J.E.; Lin, Z.M. Toxicokinetics, dose-response, and risk assessment of nanomaterials: Methodology, challenges, and future perspectives. *WIREs Nanomed. Nanobiotechnol.* **2022**, *14*, e1808. [CrossRef]
13. Hong, F.S.; Yu, X.H.; Wu, N.; Zhang, Y.Q. Progress of in vivo studies on the systemic toxicities induced by titanium dioxide nanoparticles. *Toxicol. Res.* **2017**, *6*, 115–133. [CrossRef]

14. Riediker, M.; Zink, D.; Kreyling, W.; Oberdorster, G.; Elder, A.; Graham, U.; Lynch, I.; Duschl, A.; Ichihara, G.; Ichihara, S.; et al. Particle toxicology and health—Where are we? *Part. Fibre Toxicol.* **2019**, *16*, 19. [\[CrossRef\]](#)
15. Bolis, V.; Busco, C.; Ciarletta, M.; Distasi, C.; Erriquez, J.; Fenoglio, I.; Livraghi, S.; Morel, S. Hydrophilic/hydrophobic features of TiO₂ nanoparticles as a function of crystal phase, surface area and coating, in relation to their potential toxicity in peripheral nervous system. *J. Colloid Interface Sci.* **2012**, *369*, 28–39. [\[CrossRef\]](#) [\[PubMed\]](#)
16. Oberdörster, G.; Maynard, A.; Donaldson, K.; Castranova, V.; Fitzpatrick, J.; Ausman, K.; Carter, J.; Karn, B.; Kreyling, W.; Lai, D.; et al. Principles for characterizing the potential human health effects from exposure to nanomaterials: Elements of a screening strategy. *Part. Fibre Toxicol.* **2005**, *2*, 8. [\[CrossRef\]](#) [\[PubMed\]](#)
17. Park, E.J.; Yi, J.; Chung, K.H.; Ryu, D.Y.; Choi, J.; Park, K. Oxidative stress and apoptosis induced by titanium dioxide nanoparticles in cultured BEAS-2B cells. *Toxicol. Lett.* **2008**, *180*, 222–229. [\[CrossRef\]](#) [\[PubMed\]](#)
18. Warheit, D.B.; Webb, T.R.; Reed, K.L.; Frerichs, S.; Sayes, C.M. Pulmonary toxicity study in rats with three forms of ultrafine-TiO₂ particles: Differential responses related to surface properties. *Toxicology* **2007**, *230*, 90–104. [\[CrossRef\]](#) [\[PubMed\]](#)
19. Murugadoss, S.; Brassinne, F.; Sebaihi, N.; Petry, J.; Cokic, S.M.; Van Landuyt, K.L.; Godderis, L.; Mast, J.; Lison, D.; Hoet, P.H.; et al. Agglomeration of titanium dioxide nanoparticles increases toxicological responses in vitro and in vivo. *Part. Fibre Toxicol.* **2020**, *17*, 10. [\[CrossRef\]](#)
20. Strobel, C.; Torrano, A.A.; Herrmann, R.; Malissek, M.; Bräuchle, C.; Reller, A.; Treuel, L.; Hilger, I. Effects of the physicochemical properties of titanium dioxide nanoparticles, commonly used as sun protection agents, on microvascular endothelial cells. *J. Nanopart. Res.* **2013**, *16*, 2130. [\[CrossRef\]](#)
21. Demir, E. A review on nanotoxicity and nanogenotoxicity of different shapes of nanomaterials. *J. Appl. Toxicol.* **2021**, *41*, 118–147. [\[CrossRef\]](#)
22. Warheit, D.B.; Brown, S.C. What is the impact of surface modifications and particle size on commercial titanium dioxide particle samples?—A review of in vivo pulmonary and oral toxicity studies. *Toxicol. Lett.* **2019**, *302*, 42–59. [\[CrossRef\]](#)
23. Westphal, G.A.; Schremmer, I.; Rostek, A.; Loza, K.; Rosenkranz, N.; Brüning, T.; Epple, M.; Bünger, J. Particle-induced cell migration assay (PICMA): A new *in vitro* assay for inflammatory particle effects based on permanent cell lines. *Toxicol. Vitro* **2015**, *29*, 997–1005. [\[CrossRef\]](#)
24. Brinker, C.J.; Scherer, G.W. *Sol-Gel Science. The Physics and Chemistry of Sol-Gel Processing*; Academic Press: Boston, MA, USA, 1990; p. 908.
25. Bargougui, R.; Bouazizi, N.; Soltan, W.; Gadri, A.; Azzouz, A.; Ammar, S. Controlled synthesis and electrical conduction properties of anatase TiO₂ nanoparticles via the polyol method. *Appl. Phys. A* **2016**, *122*, 309. [\[CrossRef\]](#)
26. Prathan, A.; Sanglao, J.; Wang, T.; Bhoomanee, C.; Ruankham, P.; Gardchareon, A.; Wongrataphisan, D. Controlled structure and growth mechanism behind hydrothermal growth of TiO₂ nanorods. *Sci. Rep.* **2020**, *10*, 8065. [\[CrossRef\]](#) [\[PubMed\]](#)
27. Yin, H.; Wada, Y.; Kitamura, T.; Kambe, S.; Murasawa, S.; Mori, H.; Sakata, T.; Yanagida, S. Hydrothermal synthesis of nanosized anatase and rutile TiO₂ using amorphous phase TiO₂. *J. Mater. Chem.* **2001**, *11*, 1694–1703. [\[CrossRef\]](#)
28. Klug, H.P.; Alexander, L.E. *X-Ray Diffraction Procedures for Polycrystalline and Amorphous Materials*; Wiley-Interscience: New York, NY, USA, 1974.
29. Han, C.; Luque, R.; Dionysiou, D.D. Facile preparation of controllable size monodisperse anatase titania nanoparticles. *Chem. Comm.* **2012**, *48*, 1860–1862. [\[CrossRef\]](#) [\[PubMed\]](#)
30. Ye, J.; Liu, W.; Cai, J.; Chen, S.; Zhao, X.; Zhou, H.; Qi, L. Nanoporous anatase TiO₂ mesocrystals: Additive-free synthesis, remarkable crystalline-phase stability, and improved lithium insertion behavior. *J. Am. Chem. Soc.* **2011**, *133*, 933–940. [\[CrossRef\]](#) [\[PubMed\]](#)
31. Dong, B.H.; Guo, Z.G.; Wang, S.M.; Song, X.L.; Zhao, L.; Lu, H.B.; Wan, L. Controlled synthesis of titanium dioxide nanocomposites with different structures and morphologies. *Appl. Mech. Mater.* **2014**, *535*, 645–649. [\[CrossRef\]](#)
32. Yan, J.; Wu, G.; Guan, N.; Li, L.; Li, Z.; Cao, X. Understanding the effect of surface/bulk defects on the photocatalytic activity of TiO₂: Anatase versus rutile. *Phys. Chem. Chem. Phys.* **2013**, *15*, 10978–10988. [\[CrossRef\]](#)
33. Kemp, T.J.; McIntyre, R.A. Mechanism of action of titanium dioxide pigment in the photodegradation of poly(vinyl chloride) and other polymers. *Prog. React. Kinet. Mech.* **2001**, *26*, 337–374. [\[CrossRef\]](#)
34. Banfield, J.F.; Veblen, D.R. Conversion of perovskite to anatase and TiO₂ (B): A TEM study and the use of fundamental building blocks for understanding relationships among the TiO₂ minerals. *Am. Mineral.* **1992**, *77*, 545–557.
35. Duhamel, M.; Rodet, F.; Delhem, N.; Vanden Abeele, F.; Kobeissy, F.; Nataf, S.; Pays, L.; Desjardins, R.; Gagnon, H.; Wisztorski, M.; et al. Molecular consequences of proprotein convertase 1/3 (PC1/3) inhibition in macrophages for application to cancer immunotherapy: A proteomic study. *Mol. Cell. Proteom.* **2015**, *14*, 2857–2877. [\[CrossRef\]](#)
36. Boyden, S. The chemotactic effect of mixtures of antibody and antigen on polymorphonuclear leucocytes. *J. Exp. Med.* **1962**, *115*, 453–466. [\[CrossRef\]](#)
37. Westphal, G.A.; Rosenkranz, N.; Brik, A.; Weber, D.; Föhring, I.; Monsé, C.; Kaiser, N.; Hellack, B.; Mattenklott, M.; Brüning, T.; et al. Multi-walled carbon nanotubes induce stronger migration of inflammatory cells in vitro than asbestos or granular particles but a similar pattern of inflammatory mediators. *Toxicol. Vitro* **2019**, *58*, 215–223. [\[CrossRef\]](#) [\[PubMed\]](#)
38. Sugapriya, S.; Sriram, R.; Lakshmi, S. Effect of annealing on TiO₂ nanoparticles. *Optik* **2013**, *124*, 4971–4975. [\[CrossRef\]](#)
39. Yoon, H.; Kim, D.; Park, M.; Kim, J.; Kim, J.; Srituravanich, W.; Shin, B.; Jung, Y.; Jeon, S. Extraordinary enhancement of UV absorption in TiO₂ nanoparticles enabled by low-oxidized graphene nanodots. *J. Phys. Chem. C* **2018**, *122*, 12114–12121. [\[CrossRef\]](#)

40. Cohen, J.M.; Teeguarden, J.G.; Demokritou, P. An integrated approach for the in vitro dosimetry of engineered nanomaterials. *Part. Fibre Toxicol.* **2014**, *11*, 20. [\[CrossRef\]](#)
41. Hinderliter, P.M.; Minard, K.R.; Orr, G.; Chrisler, W.B.; Thrall, B.D.; Pounds, J.G.; Teeguarden, J.G. ISDD: A computational model of particle sedimentation, diffusion and target cell dosimetry for in vitro toxicity studies. *Part. Fibre Toxicol.* **2010**, *7*, 36. [\[CrossRef\]](#)
42. Karcher, S.; Willighagen, E.L.; Rumble, J.; Ehrhart, F.; Evelo, C.T.; Fritts, M.; Gaheen, S.; Harper, S.L.; Hoover, M.D.; Jeliaskova, N.; et al. Integration among databases and data sets to support productive nanotechnology: Challenges and recommendations. *Nanoimpact* **2018**, *9*, 85–101. [\[CrossRef\]](#)
43. Patel, S.; Kim, J.; Herrera, M.; Mukherjee, A.; Kabanov, A.V.; Sahay, G. Brief update on endocytosis of nanomedicines. *Adv. Drug Deliv. Rev.* **2019**, *144*, 90–111. [\[CrossRef\]](#)
44. Carrillo-Carrion, C.; Bocanegra, A.I.; Arnaiz, B.; Feliu, N.; Zhu, D.C.; Parak, W.J. Triple-labeling of polymer-coated quantum dots and adsorbed proteins for tracing their fate in cell cultures. *ACS Nano* **2019**, *13*, 4631–4639. [\[CrossRef\]](#)
45. Foroozandeh, P.; Aziz, A.A. Insight into cellular uptake and intracellular trafficking of nanoparticles. *Nanoscale Res. Lett.* **2018**, *13*, 339. [\[CrossRef\]](#)
46. Zhang, S.; Gao, H.; Bao, G. Physical principles of nanoparticle cellular endocytosis. *ACS Nano* **2015**, *9*, 8655–8671. [\[CrossRef\]](#)
47. Kuhn, D.A.; Vanhecke, D.; Michen, B.; Blank, F.; Gehr, P.; Petri-Fink, A.; Rothen-Rutishauser, B. Different endocytotic uptake mechanisms for nanoparticles in epithelial cells and macrophages. *Beilstein J. Nanotechnol.* **2014**, *5*, 1625–1636. [\[CrossRef\]](#) [\[PubMed\]](#)
48. Sokolova, V.; Loza, K.; Knuschke, T.; Heinen-Weiler, J.; Jastrow, H.; Hasenberg, M.; Buer, J.; Westendorf, A.M.; Gunzer, M.; Epple, M. A systematic electron microscopic study on the uptake of barium sulphate nano-, submicro-, microparticles by bone marrow-derived phagocytosing cells. *Acta Biomater.* **2018**, *80*, 352–363. [\[CrossRef\]](#) [\[PubMed\]](#)
49. Nakayama, M. Macrophage recognition of crystals and nanoparticles. *Front. Immunol.* **2018**, *9*, 103. [\[CrossRef\]](#) [\[PubMed\]](#)
50. Mohning, M.P.; Thomas, S.M.; Barthel, L.; Mould, K.J.; McCubbrey, A.L.; Frasc, S.C.; Bratton, D.L.; Henson, P.M.; Janssen, W.J. Phagocytosis of microparticles by alveolar macrophages during acute lung injury requires MerTK. *Am. J. Physiol. Lung Cell Mol. Physiol.* **2018**, *314*, L69–L82. [\[CrossRef\]](#)
51. Wiemann, M.; Vennemann, A.; Sauer, U.G.; Wiench, K.; Ma-Hock, L.; Landsiedel, R. An in vitro alveolar macrophage assay for predicting the short-term inhalation toxicity of nanomaterials. *J. Nanobiotechnol.* **2016**, *14*, 16. [\[CrossRef\]](#)
52. Loza, K.; Schremmer, I.; Bünger, J.; Westphal, G.A.; Köller, M.; Epple, M.; Sengstock, C. Barium sulfate micro- and nanoparticles as bioinert reference material in particle toxicology. *Nanotoxicology* **2016**, *10*, 1492–1502. [\[CrossRef\]](#)
53. Kersting, M.; Olejnik, M.; Rosenkranz, N.; Loza, K.; Breisch, M.; Rostek, A.; Westphal, G.; Bünger, J.; Ziegler, N.; Ludwig, A.; et al. Subtoxic cell responses to silica particles with different size and shape. *Sci. Rep.* **2020**, *10*, 21591. [\[CrossRef\]](#)
54. Olejnik, M.; Breisch, M.; Sokolova, V.; Loza, K.; Prymak, O.; Rosenkranz, N.; Westphal, G.; Bünger, J.; Köller, M.; Sengstock, C.; et al. The effect of short silica fibers (0.3 μm –3.2 μm) on macrophages. *Sci. Total Environ.* **2021**, *769*, 144575. [\[CrossRef\]](#)
55. Olejnik, M.; Kersting, M.; Rosenkranz, N.; Loza, K.; Breisch, M.; Rostek, A.; Prymak, O.; Schürmeyer, L.; Westphal, G.; Köller, M.; et al. Cell-biological effects of zinc oxide spheres and rods from the nano- to the microscale at sub-toxic levels. *Cell Biol. Toxicol.* **2021**, *37*, 573–593. [\[CrossRef\]](#)

Disclaimer/Publisher’s Note: The statements, opinions and data contained in all publications are solely those of the individual author(s) and contributor(s) and not of MDPI and/or the editor(s). MDPI and/or the editor(s) disclaim responsibility for any injury to people or property resulting from any ideas, methods, instructions or products referred to in the content.